Residual stress and mechanical strength of $Ce_{0.8}Gd_{0.2}O_{2-\delta}$-$FeCo_2O_4$ dual phase oxygen transport membranes

Fanlin Zeng[1,2,*], Jürgen Malzbender[1], Stefan Baumann[1], Arian Nijmeijer[2], Louis Winnubst[2], Olivier Guillon[1,4], Ruth Schwaiger[1,3,4], Wilhelm A. Meulenberg[1,2]

[1]Forschungszentrum Jülich GmbH, Institute of Energy and Climate Research (IEK), 52425 Jülich, Germany
[2]University of Twente, Faculty of Science and Technology, Inorganic Membranes, P.O. Box 217, 7500 AE Enschede, The Netherlands
[3]RWTH Aachen University, Chair of Energy Engineering Materials, 52056 Aachen, Germany
[4]Jülich Aachen Research Alliance, JARA-Energy, 52425, Jülich, Germany

Abstract

$Ce_{0.8}Gd_{0.2}O_{2-\delta}$-$FeCo_2O_4$ membranes, benefiting from their excellent chemical stability, exhibit a broad application potential in oxygen-consuming industrial processes running in harsh environments. For long-term reliable operation, the membrane needs to possess sufficient mechanical strength. This paper characterizes the typical aspects that challenge the mechanical stability of the sintered membrane, including composition and microstructural defects as well as residual stress and residual stress gradients. It is revealed that mechanical strengths of the sintered membranes increase with decreasing iron cobalt spinel content, that the high iron cobalt spinel content induces microcracks, and that high residual tensile stress gradually decreases from the as-sintered surface to the bulk. Although the residual tensile stress can be reduced by applying an extensive elevated temperature dwell time during cooling, it is suggested to limit the iron cobalt spinel content to a nominal value of 15 wt% to eliminate the residual tensile stress while maintaining a high mechanical strength.

Keywords: dual phase ceramic composite, oxygen transport membrane, mechanical strength, residual stress.

1. Introduction

Ceramic oxygen transport membranes possess substantial economic and environmental benefits for industrial processes related to high purity oxygen separation and production [1-3], partial oxidation of hydrocarbons [4-6], and oxy-combustion [7-9]. Single phase perovskite membranes, such as $Ba_{0.5}Sr_{0.5}Co_{0.8}Fe_{0.2}O_{3-\delta}$ [10], and $La_{0.6}Sr_{0.4}Co_{0.2}Fe_{0.8}O_{3-\delta}$ [11], exhibit high oxygen permeation fluxes but suffer from chemical and thermo-mechanical instabilities under practical application-relevant conditions [12-19]. By contrast, it has been verified that dual phase membranes consisting of ion-conducting phase(s) and electron-conducting phase(s) possess excellent chemical stability under harsh application environments [20-28]. The CGO fluorite is often chosen as the ionic conducting phase for dual phase membranes because of its high ionic conductivity [29], as well as high chemical stability [20-22, 24, 28, 30-34]. Spinel oxides, e.g., $Fe_xCo_{3-x}O_4$ (x = 1 or 2), $NiFe_2O_4$, and $Mn_{1.5}Co_{1.5}O_4$, have been widely used as electron-conducting phases for CGO-based dual phase membranes to realize high mixed ionic-electron conductivity [20, 35-38]. As an example, 85 wt% $Ce_{0.8}Gd_{0.2}O_{2-\delta}$-15 wt% $FeCo_2O_4$ membrane, which contains an ion-conducting phase-$Ce_{1-x}Gd_xO_{2-\delta}$ ($0< x <0.2$) (CGO) and two electron-conducting phases-

*Corresponding author
Email: f.zeng@fz-juelich.de
Tel.: ++49-2461-619399
Fax: ++49-2461-612455

$Fe_yCo_{3-y}O_4$ ($0 < y < 2$) (FCO) and $Gd_{0.85}Ce_{0.15}Fe_{0.75}Co_{0.25}O_3$ (GCFCO) [20, 39, 40], has been shown to be chemically and functionally stable in CO_2- and SO_2-containing gas mixtures at 850 °C over at least 200 h under an oxygen partial pressure gradient [20, 41].

For the long-term safe operation of oxygen transport membranes under application-relevant conditions, in addition to oxygen permeation flux and chemical stability also the mechanical strength needs to be considered as one critical aspect [15, 42]. However, only a few studies have yet focused on the mechanical strength of dual phase membranes [40, 43-46].

Microstructural defects, e.g., cracks, impurities, inhomogeneities and voids, are known to be typical fracture origins of ceramic materials [47]. In addition, residual stresses and residual stress gradients also affect the fracture behavior of ceramic materials [48]. A residual tensile stress can lead to a decrease of the apparent mechanical strength by inducing cracks and increasing the stress intensity at potential fracture origins. Compositional and/or stoichiometric gradients over the thickness of the ceramic sample, which can be induced by inhomogeneous phase transformations and/or stoichiometric differences, may result in residual stress gradients [48]. Dual phase membranes, for example, comprising fluorite and Co-containing spinel phases, have typical sintering temperatures between 1200 °C and 1400 °C [20, 35-37], which is a temperature range where a CoO rock salt phase exists [40]. The spinel phase results from a phase transformation of the rock salt phase during cooling after sintering [40]. This phase transformation process appears to be slower in the bulk than at the surface of the ceramic due to the presence of the CGO and GCFCO phases, hence, a small amount of rock salt was reported to remain in the bulk of 50 wt% $Ce_{0.8}Gd_{0.2}O_{2-\delta}$-50 wt% $FeCo_2O_4$ membranes even after applying a slow cooling rate of 0.5 K/min in the critical temperature range of 900 °C-800 °C [39, 49]. In addition to the different amounts of the rock salt phase over the membrane thickness, the crystal structure of the fluorite phase (CGO) in 50 wt% $Ce_{0.8}Gd_{0.2}O_{2-\delta}$-50 wt% $FeCo_2O_4$ and 85 wt% $Ce_{0.8}Gd_{0.2}O_{2-\delta}$-15 wt% $FeCo_2O_4$ membranes also varies between the surface and the bulk materials: the lattice constant of CGO in the bulk is larger than that at the surface, which indicates that the oxygen non-stoichiometry in CGO in the bulk is higher than that at the surface [50]. Such oxygen stoichiometry variations between surface and bulk are likely origins of residual tensile stresses that gradually decrease from surface to bulk [50].

The current work focuses on the characterization of the residual stress and its effect on the fracture strength as well as on the development of thermal processing steps to alleviate any detrimental residual stresses, i.e., tensile stresses, for $Ce_{0.8}Gd_{0.2}O_{2-\delta}$-$FeCo_2O_4$ dual phase membranes. The microstructural, compositional and crystal-structure variations across the disc-shaped membrane were investigated in detail as potential causes of residual stress. The residual stress and residual stress gradient within the membrane were analyzed by X-ray diffraction (based on the $\sin^2\psi$ method) and indentation. The relation between fracture strength and residual stress is discussed, aided by fractographic analysis of fractured membranes that experience different residual stress states.

2. Experimental

$Ce_{0.8}Gd_{0.2}O_{2-\delta}$-$FeCo_2O_4$ composites were synthesized by solid-state reaction based on a one-step thermal processing. Stoichiometric amounts of $Ce_{0.8}Gd_{0.2}O_{2-\delta}$ (Treibacher Industrie AG, 99%), Co_3O_4 (Alfa Aesar,

99.7%) and Fe_2O_3 (Sigma-Aldrich, 99%) were mixed as precursor powder mixtures to prepare three different nominal weight ratios of $Ce_{0.8}Gd_{0.2}O_{2-\delta}$ to $FeCo_2O_4$, being 50:50, 70:30 and 85:15; the Co/Fe mole ratio was fixed at a value of two to form $FeCo_2O_4$ nominally [40]. The powder mixtures, ethanol and zirconia balls were filled up to relative ~30 vol% in a polyethylene bottle and milled on a roller bench. Other details regarding milling parameters and procedures can be found in our previous work [40]. The ball-milled powder mixtures were then dried at 75 °C for 3 days and subsequently uniaxially pressed into discs with diameters of 20 mm using a pressure of 19 MPa [40, 49]. The obtained discs were sintered in air at 1200 °C for 10 hours at a heating rate of 3 K/min. Two different cooling procedures were applied to complete the oxidization of the CoO rock salt phase [51-53]. The first one included a slow cooling step of 0.5 K/min between 900 °C and 800 °C, while the cooling rate for the other temperature ranges was 3 K/min. Three composites, which are referred to as 50CF, 70CF and 85CF in the following, were obtained with this cooling procedure. The numbers of the abbreviations correspond to the nominal fractions of $Ce_{0.8}Gd_{0.2}O_{2-\delta}$ content in the staring powder mixtures. The second cooling procedure included an extended dwelling step at 850 °C for 100 hours, while the cooling rate for the entire temperature range was 3 K/min. This cooling procedure was only applied for the sintering of 50CF, which will be referred to as dwelled-50CF.

The materials below the as-sintered surfaces of the 1 mm thick sintered discs were gradually exposed by controlled grinding and polishing steps, as outlined in detail in our previous work [50]. Residual stresses potentially induced by the grinding were removed by multiple fine-polishing steps to achieve a mirror finish [54]. In this way, two materials' subsurface regions at respective depths of ~30 and ~300 µm below the original as-sintered surface, termed in the following shallow sub-surface and deep sub-surface, respectively, were exposed. For the sample 50CF, both shallow and deep sub-surface were prepared, while for dwelled-50CF, 70CF and 85CF, only the deep sub-surfaces were prepared.

The crystallographic structure was characterized by X-ray diffraction (XRD) (Empyrean, Malvern Panalytical Ltd) for all composites. The instrument was equipped with a Cu long fine focus tube (40 kV / 40 mA), Bragg-Brentano^{HD} mirror (divergence = 0.4°), and PIXcel3D detector (1D-mode, active length = 3.35°, 255 channels).

Microstructures were assessed by scanning electron microscopy (SEM) (Merlin, Carl Zeiss Microscopy, Oberkochen, Germany). The porosity was estimated as the area fraction of pores using the software ImageJ [55].

The residual stresses (σ_r) within individual phases at different surfaces, including the as-sintered surfaces and deep sub-surfaces of all composites (i.e., 50CF, dwelled-50CF, 70CF, and 85CF), and the shallow sub-surface of 50CF, were determined by XRD based on the $\sin^2\psi$ method [56]. The diffraction peaks at high 2θ angles (>85°) were recorded providing sufficient intensity for analysis using a Philips MRD Pro diffractometer with Cr-K_α (35 kV / 50 mA) radiation. Lattice spacings (d) of crystal planes CGO(311), FCO(440), GCFCO(133) and CoO(220) were derived based on the diffraction peaks obtained at different angles (ψ). For a crystal plane experiencing a uniform stress state, the lattice spacing (d) is in general approximately linearly proportional to $\sin^2\psi$ [56]. The σ_r value was calculated for the different crystal planes representing the residual stresses in the individual phases [56]:

$$\sigma_r = \frac{E}{\nu + 1} \cdot \frac{1}{d_{ref}} \cdot \frac{\partial d_\psi}{\partial \sin^2 \psi} \quad (1)$$

where E and ν are elastic moduli and Poisson's ratios; d_ψ is lattice spacing measured with an inclined angle of ψ, d_{ref} the lattice spacing in a stress-free sample as a reference. Assuming that the lattice of a phase exhibits isotropic elasticity, the E value of the investigated crystal plane was estimated to be equal to the average E values determined from nanoindentations into individual grains, as described in our previous work [49]. The ν was assumed to be 0.3, which is a typical value of ceramics [57].

The indentation method was applied to estimate the average residual stresses at the as-sintered surfaces for 50CF and dwelled-50CF [58]. Assuming that the indentation crack is shorter than the thickness of the layer exhibiting a residual stress gradient, Vickers indentations at loads of 0.245 N and 1 N were imprinted using a macro indentation machine (Micromet® 1, Buehler Ltd). At each load, five indentations with a distance of 500 µm in-between were conducted while avoiding obvious microstructural defects, e.g., pores and microcracks. The critical stress intensity factors (K_C) of an indentation crack with a c/a value greater than 2.5 (a and c are half-diagonal and crack length of the indent, respectively) was calculated by [59]:

$$K_C = 0.016 \cdot \left(\frac{E}{H}\right)^{0.5} \cdot \left(\frac{P}{c}\right)^{1.5} \quad (2)$$

where E and H are elastic modulus and hardness, respectively, as taken from our previous work [49], and P is the indentation load.

The K_C obtained at a surface experiencing residual stress is composed of two terms [58]:

$$K_C = K_{IFR} - K_{res} \quad (3)$$

where K_{IFR} denotes indentation fracture resistance (or indentation fracture toughness), which can be considered to be equal to K_C value at a stress-free surface, and K_{res} represents the K_C value for a crack in a residual stress field, given by [58]:

$$K_{res} = Y \cdot \sigma_r \cdot \sqrt{c} \quad (4)$$

where Y is the crack geometry factor with a value approximately equal to $1.12\sqrt{\pi}$ for a half-penny shaped crack [60, 61].

The fracture strength, i.e., being in the current work defined as the average fracture stress, was determined by ring-on-ring bending tests using an electromechanical testing machine (Instron 1362, Lebow Ltd) following the general procedure outlined in ASTM C1499-05 [62]. Either the as-sintered surface or the deep sub-surface was in tension during the test. Loading and supporting rings with diameters of 3.43 and 9.99 mm, respectively, were used. The stress rate was 20 MPa/s [50]. Five as-sintered specimens were tested for each composite. To test with the deep sub-surface in tension, five as-sintered 50CF discs were ground and polished at one side to obtain deep sub-surfaces. The specimen thickness after the surface layer removal was less uniform than before (the average standard deviation of all specimens was ~29 µm). Hence, the fracture stress of each ground and polished 50CF was

calculated using the smallest and largest thickness measured within the effectively tested area. The fracture stress (σ_f) was derived from equation (5) [40, 50, 62], and averaged for each composite.

$$\sigma_f = \frac{3F}{2\pi \cdot t^2} \cdot \left[(1-\nu) \cdot \frac{r_s^2 - r_l^2}{2r_d^2} + (1+\nu) \cdot \ln \frac{r_s}{r_l} \right] \quad (5)$$

where F is the fracture force; r is the radius, t the thickness; subscripts s, l, and d denote the support ring, loading ring, and the tested disc, respectively.

The fracture surfaces were investigated using SEM to reveal the likely fracture origins. The measured fracture origin size (C), i.e., the equivalent radius of circular/semicircular origin or minor axis length of elliptical/semielliptical origin, was compared with the values estimated by [40, 50]:

$$\sqrt{C} = \frac{K_{IC}}{Y \cdot \sigma} \quad (6)$$

where σ is the stress at the fracture origin. Several Y values for origins with different shapes, in addition to the Y value for a half-penny shaped crack (see also above), are given in ASTM C1322-15 [47].

3. Results and discussion

3.1 Microstructure

The microstructures of the as-sintered surface, the shallow and deep sub-surface of 50CF as characterized by SEM are presented in Figure 1. The different phases can be distinguished by their different greyscale level. According to our previous electron backscatter diffraction phase mapping studies on the same composite with an identical microstructure, a CoO rock salt phase exists in the deep sub-surface of the sintered 50CF [49]. This CoO cannot be distinguished from the FCO phase due to a similar contrast in the BSEM micrographs [49]. Apparently, in the deep sub-surface of 50CF, the CoO rock salt phase needs a longer time to be oxidized into the spinel during cooling, while at the surface of 50CF, the oxidization of the CoO rock salt phase can be completed upon exposure to the excess oxygen in air [50]. As confirmed by XRD patterns (Supplementary, Figure S2), the CoO only exists in the shallow and deep sub-surface regions of 50CF, while CGO, FCO and GCFCO can be found in all investigated surface regions. Thus, the black grains at the as-sintered surface, as shown in Figure 1(a), are FCO spinel grains, while the ones at the shallow and deep sub-surface, as shown in Figure 1(b,c), can be either CoO or FCO grains. The incomplete oxidization of CoO indicates oxygen deficiency within the deep sub-surface of 50CF. The grey and light grey grains in the deep sub-surface of the composites are CGO and GCFCO grains (see Figure 1(b,c)) [49], respectively. However, CGO and GCFCO grains cannot be distinguished at the as-sintered surfaces. No significant phase composition variations across the discs are observed. Furthermore, a considerable number of long microcracks were observed at the as-sintered surface of 50CF (see Figure 1(a)), which possibly also propagate towards the shallow sub-surface (see Figure 1(b)) and are not visible anymore at the deep sub-surface (see Figure 1(c)).

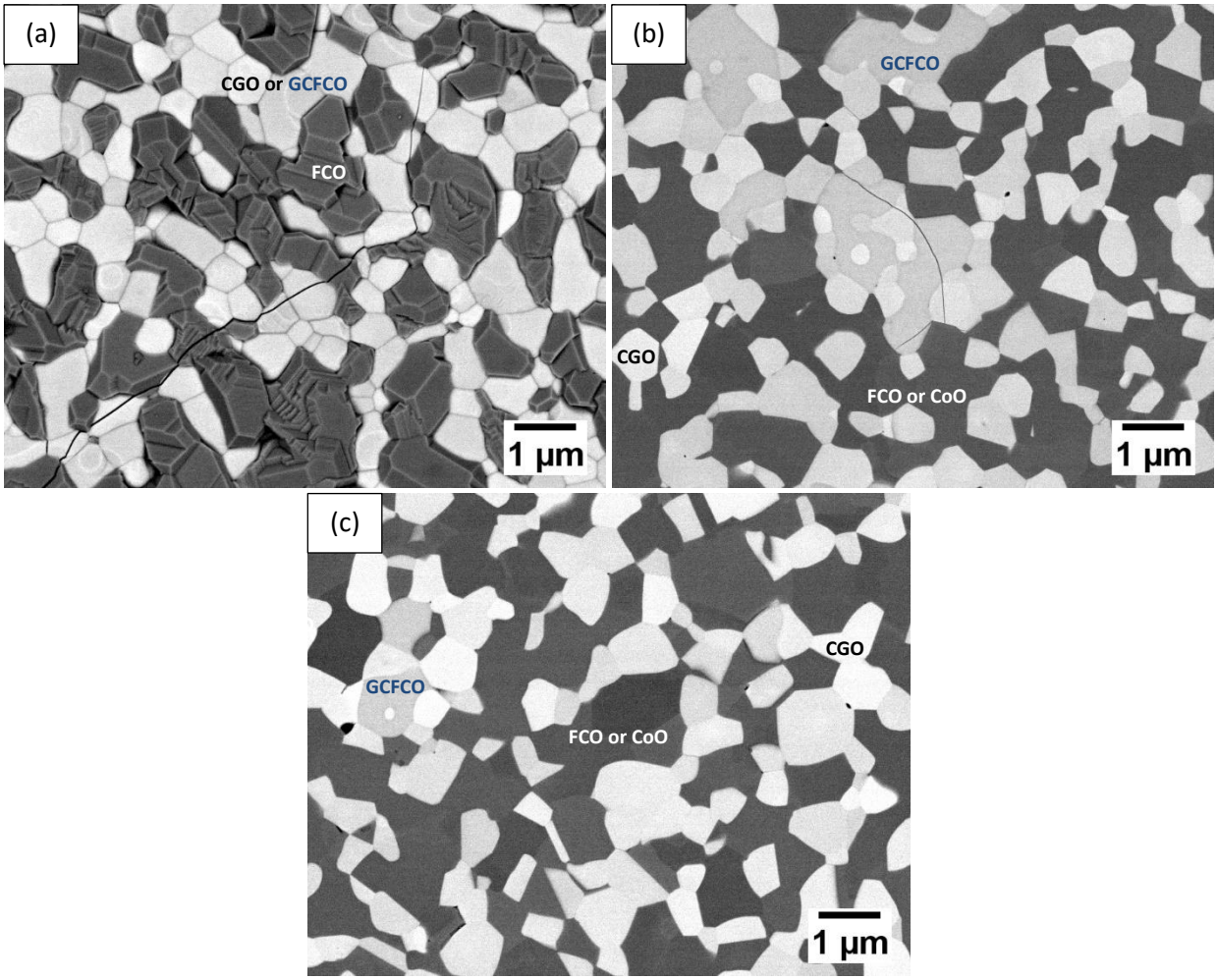

Figure 1 BSEM micrographs of (a) the as-sintered surface, (b) the shallow sub-surface, and (c) the deep sub-surface of 50CF.

For 70CF and 85CF, it was reported that the CoO phase did not residual in the deep sub-surface after sintering [49]. Hence, the black grains at the as-sintered and deep sub-surfaces, as shown in Figure 2 for 85CF as examples, are FCO spinel grains. Besides, 70CF and 85CF appear to be free of microcracks for both the as-sintered and deep sub-surfaces, as, e.g., shown in Figure 2 for 85CF. The individual phases in 70CF and 85CF show no significant volume variations regarding phase content across the sintered discs.

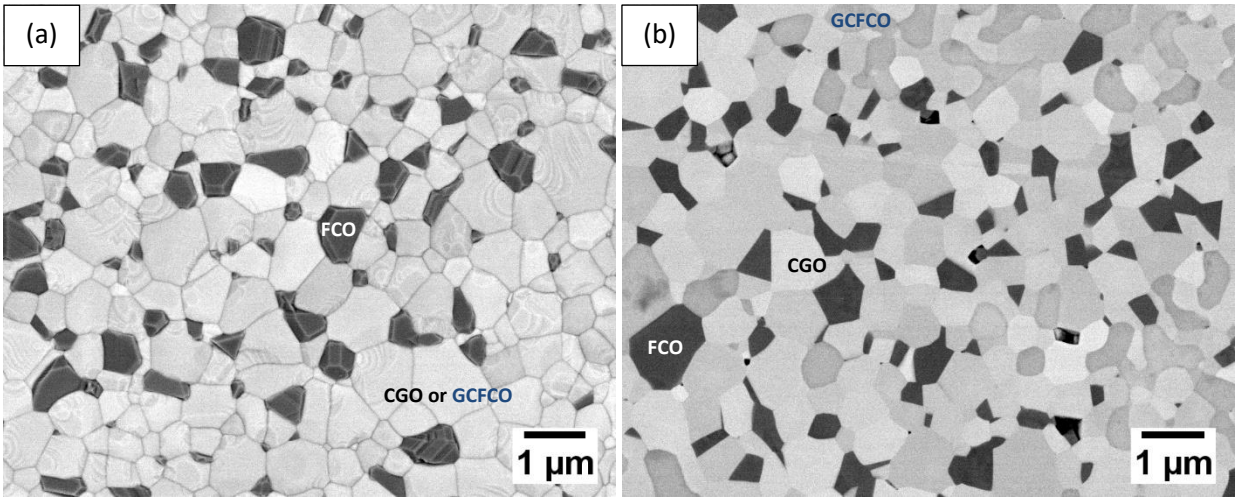

Figure 2 BSEM micrographs of (a) the as-sintered surface, and (b) the deep sub-surface of 85CF.

For dwelled-50CF, no microcracks are visible at the as-sintered surface and deep sub-surface, as illustrated in Figure S2. Furthermore, the CoO phase in the deep sub-surface is fully oxidized into the spinel phase, as confirmed by the XRD patterns (see Figure S1).

3.2 Lattice constants

The lattice constants of CGO, GCFCO and CoO as obtained at the as-sintered surfaces and deep sub-surfaces are compared in the following for all composites, while it was not possible to determine one lattice constant for FCO due to the variation of the cobalt-to-iron ratios of FCO [49].

For 50CF, the lattice constants of CGO and GCFCO in the deep sub-surface are slightly larger than the one at the as-sintered surface (see Figure 3 and Table S1). The different lattice constants might indicate differences in the oxygen stoichiometry. The lower oxygen stoichiometry in CGO and GCFCO are possibly caused by an oxygen deficiency within the deep sub-surface of 50CF, as supported by the existence of the CoO phase that did not oxidize into the spinel during cooling.

For 70CF and 85CF, the lattice constants of CGO and GCFCO share similar values at the as-sintered surfaces and deep sub-surfaces (see Figure 3 and Table S1). However, according to our previous work on 85CF containing larger FCO grains [50], the lattice constant of CGO is marginally larger at the deep sub-surface than at the as-sintered surface. This indicates that differences in the lattice constant of CGO over the cross section of 85CF cannot be observed due to the reduced grain size of FCO.

For dwelled-50CF, the lattice constants of CGO are almost identical (~5.412 Å) at the as-sintered surface and the deep sub-surface, as shown in Figure S1. And the CoO appears to be absent within the deep sub-surface. Therefore, the potential oxygen stoichiometry deviation across the sample can be smoothed out after the dwelling step.

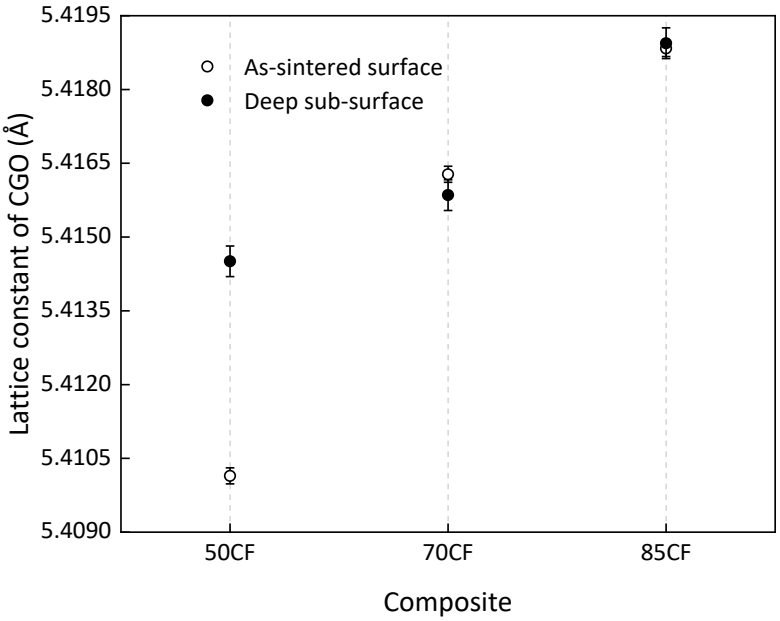

Figure 3 Lattice constants of CGO at the as-sintered surfaces and deep sub-surfaces of the different composites.

3.3 Residual stress

3.3.1 XRD

For 50CF, at the as-sintered surface, the lattice spacings of CGO(311) and FCO(440) exhibit a linear dependency on $\sin^2\psi$, as shown in Figure 4. Residual tensile stresses were determined from the corresponding positive slopes according to equation (1). Due to the low intensity of the associated diffraction peaks, it was not possible to directly assess the residual stress associated with the GCFCO phase. Note, the GCFCO phase, with a volume fraction of only ~6 vol%, distributes as isolated islands surrounded by the other phases [63], and it possesses a thermal expansion coefficient comparable to that of CGO and/or FCO (~12 × 10^{-6} K^{-1}) [50]. Hence, the GCFCO phase is expected also to exhibit residual tensile stress. It can be concluded that the entire as-sintered surface exhibits a residual tensile stress. By contrast, at the shallow sub-surface, measured d values of CGO(311) and FCO(440) are almost independent of the $\sin^2\psi$ values (see Figure S3), suggesting an almost stress-free state of the shallow sub-surface. At the deep sub-surface, the d of CGO(311) decreases with $\sin^2\psi$ values; the linear fitting yields a negative slope with relatively large uncertainty, which indicates a small compressive stress value (see Figure 5). The d values of FCO(440) and CoO(220) are almost independent of $\sin^2\psi$ (see Figure S4), suggesting a stress-free state for FCO and CoO at the deep sub-surface. Since the content of CGO in 50CF is lower than 50 vol% [49], the average stress in the deep sub-surface of 50CF appears to be negligible. Therefore, it can be confirmed that a residual stress gradient across the 50CF disc exists, which can be attributed to differences in lattice shrinkage at the surface and the deep sub-surface. The lattice shrinkage during cooling can be expected to be more pronounced at the surface than in the deep sub-surface, since more oxygen vacancies are present in the deep sub-surface than at the surface after

sintering. This is indeed supported by our investigations showing that the lattice constant of CGO and GCFCO is greater at the deep sub-surface than at the as-sintered surface (see Figure 3 and Table S1).

For 70CF, d of CGO(311) and FCO(440) at the as-sintered surface slightly increase with $\sin^2\psi$ values in a nonlinear manner (see Figure 4), suggesting an almost stress-free as-sintered surface [56].

For 85CF, it has been difficult to analyze the residual stress of the FCO phase due to the low intensity of the associated diffraction peaks, the peak broadening, and the overlapping induced by the variation of Co-to-Fe ratio [50]. However, the diffraction peaks of CGO and GCFCO exhibited sufficient intensities for residual stress analysis. At the as-sintered surface, as can be seen from Figure 4(a), a linear dependency of d on $\sin^2\psi$ values is observed for CGO(311) in 85CF being an indication of a relatively small residual compressive stress. This small compressive stress was confirmed by another set of XRD measurements for CGO(331) yielding a compressive stress value of ~74 ± 4 MPa, as shown in Figure S5(a). Note, in Figure S5(b), the lattice spacings of GCFCO(133) decrease with increasing $\sin^2\psi$ values in a nonlinear manner, indicating a rather inhomogeneous strain distribution within the GCFCO grains. At the deep sub-surface, as revealed in Figure 5, the linear dependency of d on $\sin^2\psi$ for CGO(311) yields a residual compressive stress that is comparable to the one measured at the as-sintered surface (see Figure 4(a)). This observation was confirmed by a second measurement for CGO(331) also indicating a compressive stress value of ~53 ± 1 MPa (see Figure S6). Thus, the CGO phase across the sintered 85CF disc experiences a rather uniform compressive stress state, indicating that no residual stress gradient exists. After a thermal annealing using the sintering program described above, CGO(311) at the deep sub-surface of 85CF experiences a residual compressive stress of ~64 ± 3 MPa (see Figure S7). Hence, the thermal annealing has not alleviated the residual compressive stress.

For dwelled-50CF, the residual tensile stresses in CGO(311) and FCO(440) at the as-sintered surface are much lower than the ones at the as-sintered surface of 50CF (see Figure 6). This suggests that the residual tensile stress in the as-sintered surface is reduced but not fully eliminated by the extensive dwelling step.

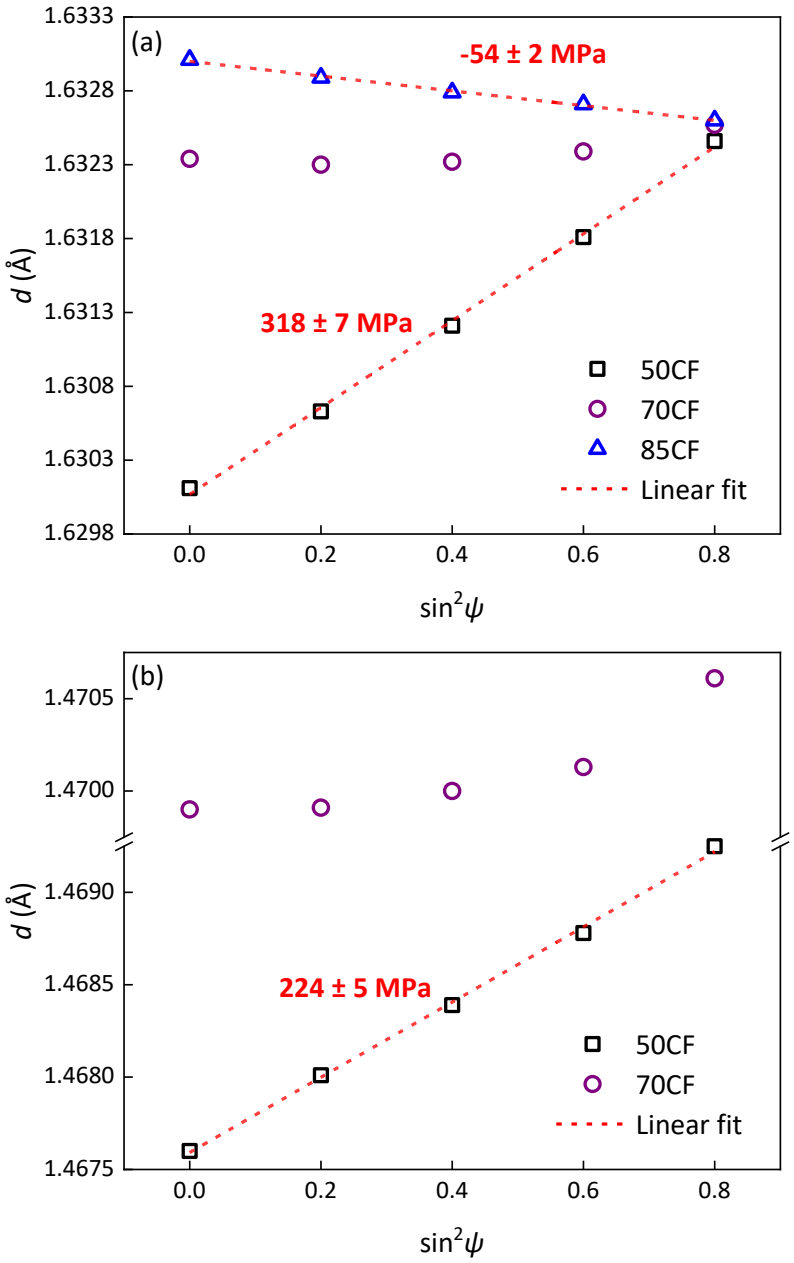

Figure 4 Dependencies of d on $\sin^2\psi$ values and residual stresses derived for (a) CGO(311) and (b) FCO(440) at the as-sintered surfaces. The residual stresses were determined from equation (1).

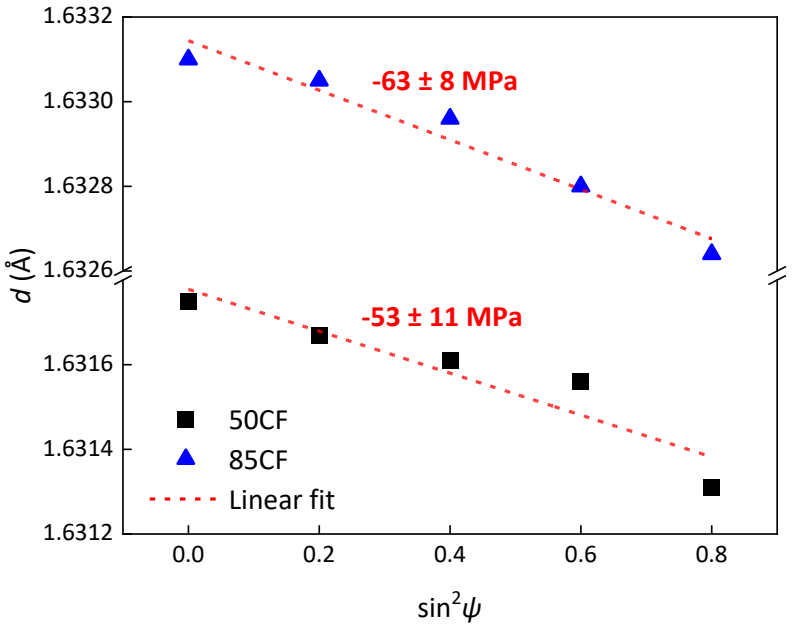

Figure 5 Dependencies of d on $\sin^2\psi$ values and residual stresses derived for CGO(311) at the deep sub-surfaces. The residual stresses were determined from equation (1).

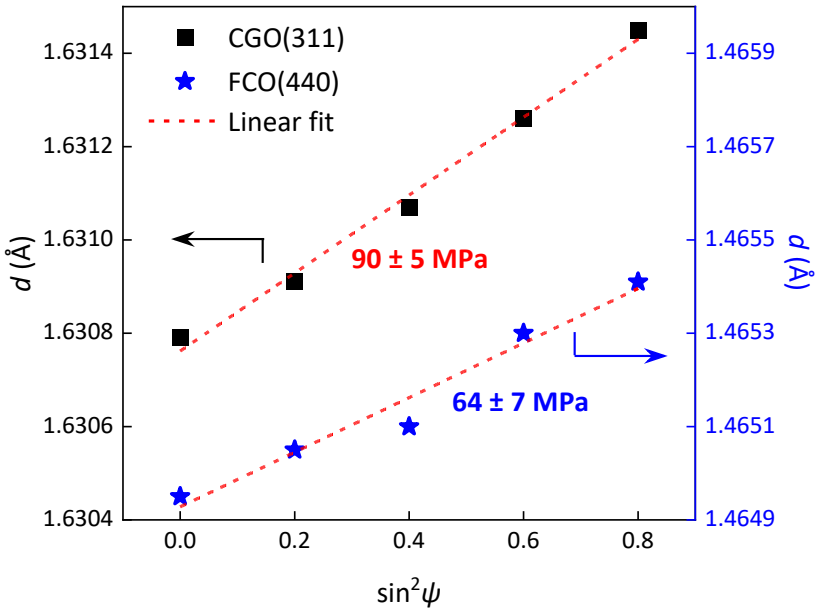

Figure 6 Dependencies of d on $\sin^2\psi$ values derived for (a) CGO(311) and (b) FCO(440) at the as-sintered surface of dwelled-50CF. The residual stress was determined according to equation (1).

3.3.2 Indentation method

Since the average penetration depth of X-rays exceeds a few microns [64], the XRD method yielded residual stress values of individual phases averaged over a thin surface layer. In contrast, the indentation method can give an average stress value for a thick surface layer including all phases present. It should be noted that a stress value cannot be obtained by the indentation method when the residual stress states between phases differ in such a way that the resulting stress is almost zero.

For 50CF and dwelled-50CF, the entire as-sintered surfaces experience the same stress state as the main phases, i.e. CGO and FCO (see Figure 4 and 6). Therefore, the indentation method was used to further investigate the residual stresses and residual stress gradients. For that purpose, K_{IFR} values, i.e. K_C values at stress-free surfaces (as can be seen from equation (3)), were firstly determined at the deep sub-surfaces, where residual stresses are negligible.

At the deep sub-surface of 50CF, well-defined indentations with ideal crack profiles were obtained after the application of a load of 1 N (see Figure 7(a)), and the c/a value was larger than 2.5 indicating a half-penny shaped crack (length equals to depth) [59, 65]. Accordingly, the K_{IFR} was derived to be ~0.82 ± 0.03 MPa·m$^{0.5}$ (see Table 1). For indentation loads of 0.245 N, cracks could hardly be generated (see Figure S8(a)). According to our previous study on the stress-free 50CF with large grains, the K_{IFR} with a value of ~0.88 ± 0.11 MPa·m$^{0.5}$ at 1 N has been almost independent of the indentation load for this type of material [50]. Thus, the expected K_{IFR} obtained at 0.245 and 1 N should be equal. Furthermore, indentation cracks, as shown in Figure 7 and Figure S9, exhibit a mainly transgranular mode with limited deflections along the grains, indicating that similar critical stress intensity factors can be expected for different grain sizes.

At the deep sub-surfaces of 70CF and 85CF, the obtained K_{IFR} values were comparable with those obtained at the deep sub-surface of 50CF (see Table 1). The K_{IFR} appears to be independent of the composition, indicating that the apparent compressive stress in CGO in 50CF and 85CF (see Figure 5) has a limited influence on the K_{IFR} values.

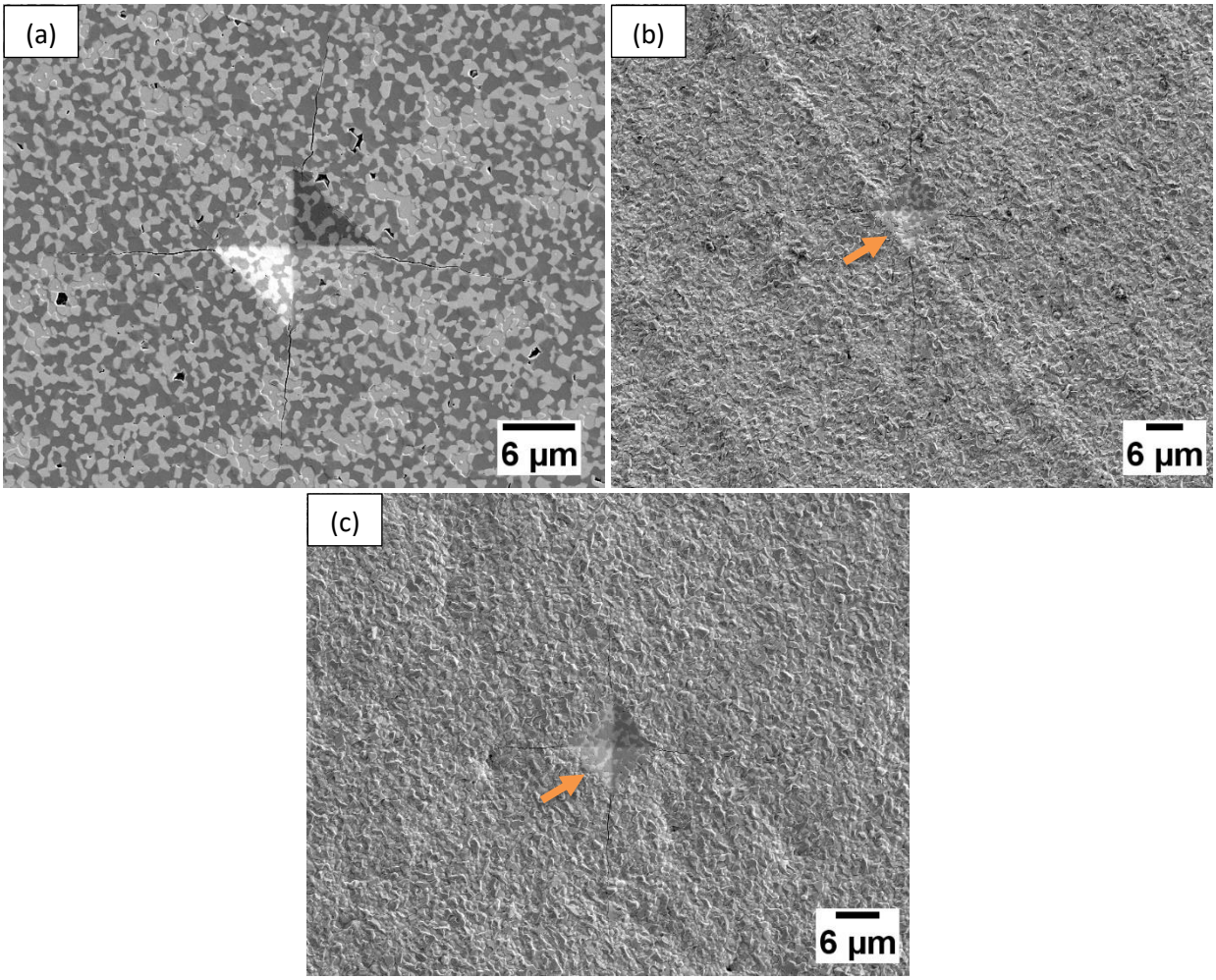

Figure 7 Vickers indentations at a load of 1N imaged by SEM on the (a) deep sub-surface of 50CF, (b) as-sintered surface of 50CF, and (c) as-sintered surface of dwelled-50CF. Imprints in (b) and (c) are marked by arrows. It should be noted that the scale bars are different.

Table 1 Critical stress intensity factors of indentation cracks derived for the deep sub-surfaces of the sintered composites.

Composite	K_C ($\approx K_{IFR}$) (MPa·m$^{0.5}$)	Reference
50CF	0.82 ± 0.03	This work
70CF	0.81 ± 0.03	
85CF	0.86 ± 0.06	[40]

Into the as-sintered surface of 50CF and dwell-50CF, imprints with well-defined crack profiles were induced by both loads (see Figure 7(b, c) and Figure S8(b, c)), from which low K_C values were calculated (see Table 2).

For the as-sintered surface of 50CF, the K_C values appear to be independent of the indentation loads and are significantly lower than the K_{IFR} values measured at the deep sub-surface of 50CF (see Table 1), indicating the significant contribution of the residual tensile stress. The residual tensile stress calculated from indentations at 0.245 N is marginally higher than the one for indentation at 1 N considering the experimental uncertainties (see Table 2). Compared to the residual tensile stress values obtained from the XRD method (see Figure 4), the stress values from the indentation method are much lower. This can probably be associated with the presence of the stress gradient, which implies that the indentation method reflects the effect of a stressed layer that is thicker than the one directly measured by the XRD method. As the indentation cracks induced by 1 N (resulting in a crack depth of ~45 ± 4 µm) are longer than the extend of the almost stress-free shallow sub-surface region (~30 µm), the residual tensile stress value derived by indentation at 1 N can be regarded as an average stress value over the whole stressed layer. The apparent indentation crack depth induced by 0.245 N (~18 ± 4 µm), however, is shorter than ~30 µm, but still exceeds the penetration depth of X-rays. The residual stress value from indentations at 0.245 N reflects the average residual tensile stress of a section of the stressed layer.

For the as-sintered surface of dwelled-50CF, the K_C value is again independent of the indentation load (see Table 2). The values are significantly larger than the ones obtained for the as-sintered surface of 50CF, but slightly lower than the K_{IFR} values determined for the deep sub-surface of 50CF (see Table 1). The apparent indentation crack depths induced by 0.245 N and 1 N are ~8 ± 1 µm and ~22 ± 1 µm, respectively. The calculated apparent residual tensile stresses are rather small and independent of the indentation load when the uncertainties are considered (see Table 2), and again lower than the residual tensile stresses obtained from XRD (see Figure 6). This suggests that the apparent indentation crack depth induced by the minimum load of 0.245 N used in the current study is already sufficient to reflect the effect of the average residual tensile stress within the entire stressed layer.

Table 2 Critical stress intensity factors of indentation cracks and residual stresses determined for the as-sintered surfaces of 50CF and dwelled-50CF.

Sample	K_C (MPa·m$^{0.5}$)		Residual stress (MPa)	
	0.245 N	1 N	0.245 N	1 N
50CF	0.24 ± 0.07	0.23 ± 0.03	69 ± 17	44 ± 6
Dwelled-50CF	0.69 ± 0.06	0.66 ± 0.05	21 ± 12	18 ± 7

3.4 Strength and fractography

For composites that were broken via the ring-on-ring test with the as-sintered surfaces in tension, the average fracture stress (strength) increases with increasing CGO content (see Figure 8). The 50CF possesses the lowest average fracture stress, which might be a result of the rather long microcracks existing in this material (see Figure 1(a)), as well as the rather high residual tensile stress (see Figure 4(a)).

When compared with the fracture stress values of other typical single-phase oxygen transport membranes, e.g., $Ba_{0.5}Sr_{0.5}Co_{0.8}Fe_{0.2}O_{3-\delta}$ (~100 MPa) [66], $La_{0.58}Sr_{0.4}Co_{0.2}Fe_{0.8}O_{3-\delta}$ (~94 MPa) [67] and $SrTi_{0.65}Fe_{0.35}O_{3-\delta}$ (~117 MPa) [60], which were determined using similar specimens, the average fracture stress of 50CF is lower, while the average fracture stress of 85CF is significantly higher.

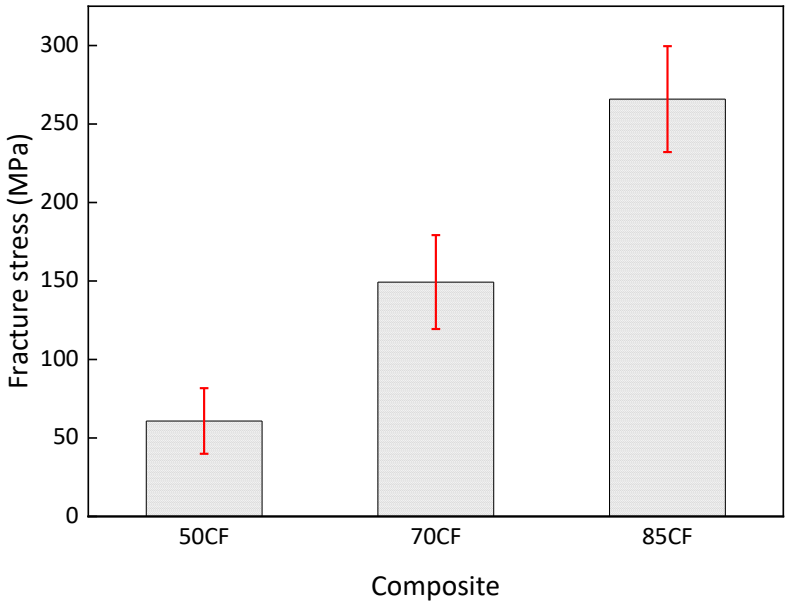

Figure 8 Average fracture stresses of composites determined for the as-sintered surfaces. The average fracture stress of 85CF has been taken from our previous work [40].

The likely fracture origins were assessed by SEM investigations on the fracture surfaces of the tested samples with the lowest fracture stresses. As reported for 85CF fractured with the as-sintered surface in tension, the fracture appears to initiate from small surface-located flaws, whose sizes are comparable with the ones estimated by equation (6) [40]. For 50CF and 70CF with the as-sintered surfaces in tension, surface-located flaws were also characterized as the likely fracture origins, as shown in Figure 9(a, b). The likely fracture origin presented in Figure 9(a) noticeably possesses a depth that is close to the length of the microcracks shown in Figure 1(a), which supports that fracture can initiate from such microcracks.

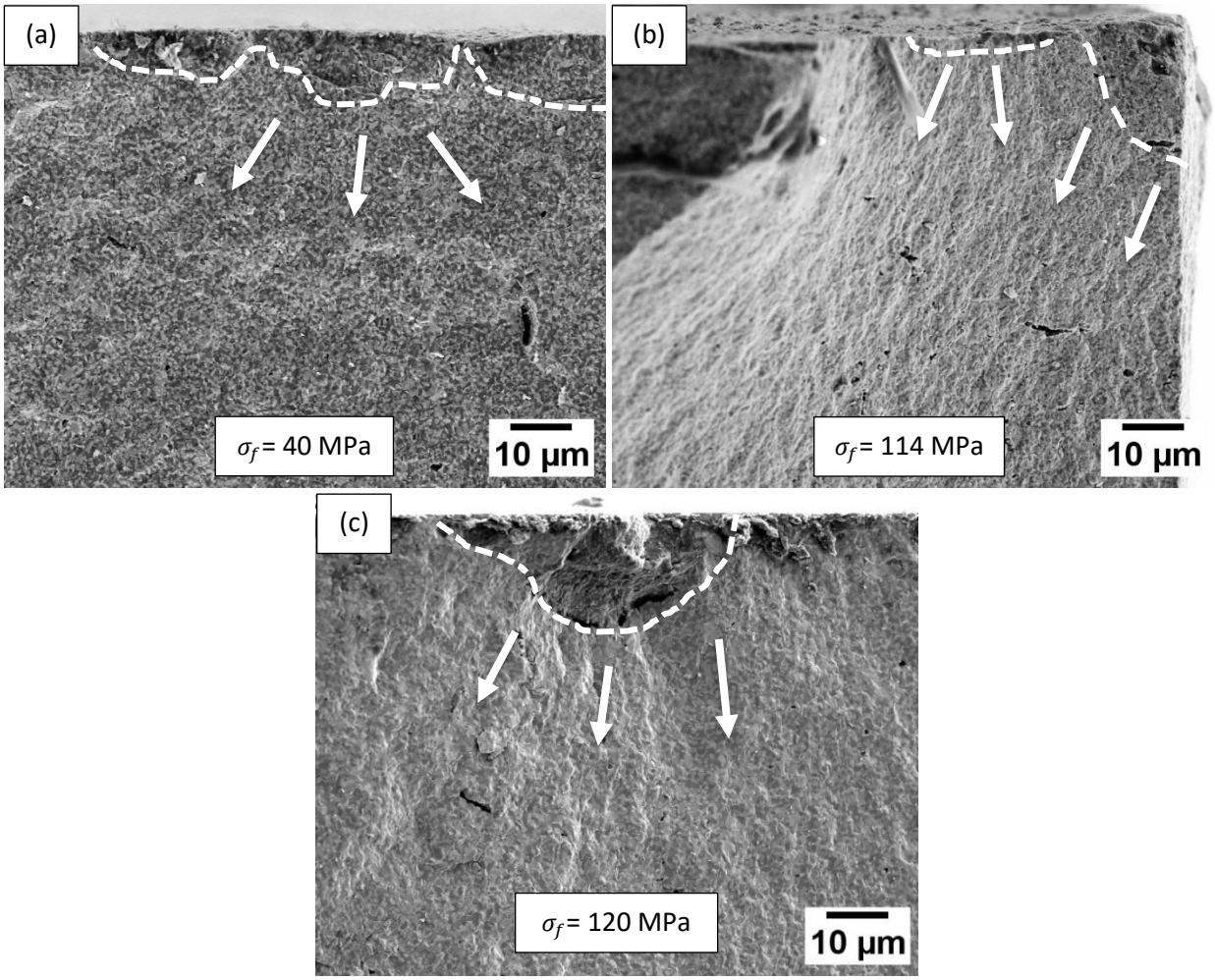

Figure 9 Fracture surfaces (SEM) of (a) 50CF, (b) 75CF fractured at the as-sintered surfaces, and (c) 50CF fractured at the deep sub-surface. Samples exhibiting the lowest fracture stresses are shown. The dashed lines represent the likely boundaries of the fracture origins. The fracture lines are indicated by the arrows.

The measured sizes of the likely fracture origins are summarized in Table 3. For comparison, the sizes of the fractured origins were also estimated using equation (6). It is assumed that the maximum stress acting at the critical defect is equal to the maximum stress applied externally during the ring-on-ring bending test, i.e., the calculated fracture stress, and that the residual stress is not contributive. For 70CF, the measured size is almost identical to the estimated one, suggesting that the sample is almost free of internal residual stress that can superimpose on the calculated fracture stress.

For 50CF fractured with the as-sintered surfaces in tension, however, the measured size of the likely fracture origin is significantly smaller than the estimated ones. The stresses used for estimating the fracture origin size might therefore be underestimated because the contribution of residual stress is not considered. Since the measured size of the likely fracture origin is close to the depth of the indentation induced crack at 0.245 N (~18 ± 4 µm), the average residual stress obtained from indentations at 0.245

N (see Table 2) is included in the calculation of fracture origin size so that the stress at the fracture origin is corrected to be equal to the sum of the internal stress (average residual stress of ~69 MPa) and the maximum applied external stress (fracture stress of ~40 MPa). The fracture origin obtained by this adjusted stress value, of ~109 MPa, is ~ 14 µm, which is almost equal to the measured fracture origin size (see Table 3). This confirms the significant influence of the residual stress on strength, which is probably a result of the fracture origin size being comparable to the thickness of the stressed layer.

Table 3 Estimated and measured fracture origin sizes.

Composite	Fractured surface	$\sigma = \sigma_f$ (MPa)	Y [47]	C (µm)		Reference
				Estimated	Measured	
50CF	As-sintered surface	40	1.99	107	14	This work
	Deep sub-surface	120	1.39	24	20	
70CF	As-sintered surface	114	1.39	26	27	
85CF	As-sintered surface	212	1.99	4	2	[40]

To further confirm the reduction of the apparent fracture stress through the presence of residual tensile stresses, the fracture stress of 50CF for the almost stress-free deep sub-surface was measured and determined to be ~ 151 ± 31 MPa, which is significantly higher than the fracture strength of 50CF measured for the as-sintered surface (~ 61 ± 21 MPa). The likely fracture origins were surface located (see Figure 9(c)). The fracture origin size, measured for the sample with the lowest fracture stress is ~20 µm (see Table 3), which is close to the one estimated without consideration of the residual stress. Hence, no significant contribution from the residual stresses on the fracture stress has been observed. The deep sub-surface can be considered free of residual stress, which agrees well with the XRD results. Thus, the fracture stress is only determined by the maximum tolerable stress intensity induced by the externally applied stress at the flaws located at the surface.

For the disc-shaped 50CF membrane, it appears to be an effective way to enhance the strength by removing the layer with residual tensile stress and microcracks, however, this is not practical for a large membrane component or a nonplanar, e.g., tubular, membrane component.

4 Conclusions

The apparent mechanical strengths (i.e., average fracture stresses) of $Ce_{0.8}Gd_{0.2}O_{2-\delta}$-$FeCo_2O_4$ membrane materials, as determined from ring-on-ring tests, increase as a function of the nominal fractions of $Ce_{0.8}Gd_{0.2}O_{2-\delta}$ content in the starting powder. The low strength of 50CF specimens appears to be a result of the presence of microcracks within the as-sintered surface that act as fracture origins, as well as high

residual tensile stress that gradually decreases from the as-sintered surface to the bulk. This residual tensile stress gradient, as determined by X-ray diffraction and indentation, is likely caused by an oxygen stoichiometry variation between the surface and bulk material. The fracture stress of 50CF is reduced significantly by the residual tensile stress since the likely fracture origins are located within the residual stress gradient zone. After removal of the material layer with residual tensile stress and microcracks, the fracture stress of 50CF is significantly improved. Besides, the residual tensile stress within the as-sintered surface of 50CF is successfully reduced by applying an extended dwelling step during cooling. However, it is recommended to limit the iron cobalt spinel content to a nominal value of 15 wt% to eliminate the residual tensile stress and obtain a membrane with small surface defects, thus, yielding a material with high mechanical strength.

Acknowledgements

Fanlin Zeng acknowledges the China Scholarship Council (CSC) for financial support. The authors gratefully acknowledge Mr. M. Ziegner, Dr. E. Wessel, Dr. D. Grüner, Mr. M. Turiaux. and Mr. S. Heinz for their contributions to structural characterization, property testing and sample preparation.

References

[1] P. Niehoff, F. Schulze-Kueppers, S. Baumann, W.A. Meulenberg, O. Guillon, R. Vassen, Fabrication of laboratory-scale planar oxygen separation membrane modules, American Ceramic Society Bulletin 94(1) (2015) 28-31.
[2] K. Zhang, J. Sunarso, Z. Shao, W. Zhou, C. Sun, S. Wang, S. Liu, Research progress and materials selection guidelines on mixed conducting perovskite-type ceramic membranes for oxygen production, RSC Advances 1(9) (2011) 1661-1676.
[3] H. Wang, S. Werth, T. Schiestel, J. Caro, Perovskite hollow-fiber membranes for the production of oxygen-enriched air, Angewandte Chemie International Edition 44(42) (2005) 6906-6909.
[4] H.J. Bouwmeester, Dense ceramic membranes for methane conversion, Catalysis Today 82(1-4) (2003) 141-150.
[5] M.T. Ravanchi, T. Kaghazchi, A. Kargari, Application of membrane separation processes in petrochemical industry: a review, Desalination 235(1-3) (2009) 199-244.
[6] W. Deibert, M.E. Ivanova, S. Baumann, O. Guillon, W.A. Meulenberg, Ion-conducting ceramic membrane reactors for high-temperature applications, Journal of Membrane Science 543 (2017) 79-97.
[7] H. Stadler, F. Beggel, M. Habermehl, B. Persigehl, R. Kneer, M. Modigell, P. Jeschke, Oxyfuel coal combustion by efficient integration of oxygen transport membranes, International Journal of Greenhouse Gas Control 5(1) (2011) 7-15.
[8] M. Ramasamy, Dual phase oxygen transport membrane for efficient oxyfuel combustion, PhD thesis, Bochum University, Bochum, Germany, 2016.
[9] X. Zhu, H. Liu, Y. Cong, W. Yang, Novel dual-phase membranes for CO_2 capture via an oxyfuel route, Chemical Communications 48(2) (2012) 251-253.
[10] S. Baumann, J.M. Serra, M.P. Lobera, S. Escolástico, F. Schulze-Küppers, W.A. Meulenberg, Ultrahigh oxygen permeation flux through supported $Ba_{0.5}Sr_{0.5}Co_{0.8}Fe_{0.2}O_{3-\delta}$ membranes, Journal of Membrane Science 377(1) (2011) 198-205.
[11] J.M. Serra, J. Garcia-Fayos, S. Baumann, F. Schulze-Küppers, W.A. Meulenberg, Oxygen permeation through tape-cast asymmetric all-$La_{0.6}Sr_{0.4}Co_{0.2}Fe_{0.8}O_{3-\delta}$ membranes, Journal of Membrane Science 447 (2013) 297-305.

[12] M. Arnold, H. Wang, A. Feldhoff, Influence of CO_2 on the oxygen permeation performance and the microstructure of perovskite-type $(Ba_{0.5}Sr_{0.5})(Co_{0.8}Fe_{0.2})O_{3-\delta}$ membranes, Journal of Membrane Science 293(1-2) (2007) 44-52.
[13] A. Waindich, A. Möbius, M. Müller, Corrosion of $Ba_{1-x}Sr_xCo_{1-y}Fe_yO_{3-\delta}$ and $La_{0.3}Ba_{0.7}Co_{0.2}Fe_{0.8}O_{3-\delta}$ materials for oxygen separating membranes under Oxycoal conditions, Journal of Membrane Science 337(1-2) (2009) 182-187.
[14] J. Gao, L. Li, Z. Yin, J. Zhang, S. Lu, X. Tan, Poisoning effect of SO_2 on the oxygen permeation behavior of $La_{0.6}Sr_{0.4}Co_{0.2}Fe_{0.8}O_{3-\delta}$ perovskite hollow fiber membranes, Journal of Membrane Science 455 (2014) 341-348.
[15] T. Ramirez-Reina, J.L. Santos, N. García-Moncada, S. Ivanova, J.A. Odriozola, Development of Robust Mixed-Conducting Membranes with High Permeability and Stability, Perovskites and Related Mixed Oxides (2016) 719-738.
[16] S. Engels, T. Markus, M. Modigell, L. Singheiser, Oxygen permeation and stability investigations on MIEC membrane materials under operating conditions for power plant processes, Journal of Membrane Science 370(1-2) (2011) 58-69.
[17] M. Schulz, R. Kriegel, A. Kämpfer, Assessment of CO_2 stability and oxygen flux of oxygen permeable membranes, Journal of Membrane Science 378(1-2) (2011) 10-17.
[18] X. Tan, N. Liu, B. Meng, J. Sunarso, K. Zhang, S. Liu, Oxygen permeation behavior of $La_{0.6}Sr_{0.4}Co_{0.8}Fe_{0.2}O_3$ hollow fibre membranes with highly concentrated CO_2 exposure, Journal of Membrane Science 389 (2012) 216-222.
[19] S.J. Benson, D. Waller, J.A. Kilner, Degradation of $La_{0.6}Sr_{0.4}Fe_{0.8}Co_{0.2}O_{3-\delta}$ in Carbon Dioxide and Water Atmospheres, Journal of the Electrochemical Society 146(4) (1999) 1305.
[20] M. Ramasamy, E.S. Persoon, S. Baumann, M. Schroeder, F. Schulze-Küppers, D. Görtz, R. Bhave, M. Bram, W.A. Meulenberg, Structural and chemical stability of high performance $Ce_{0.8}Gd_{0.2}O_{2-\delta}$-$FeCo_2O_4$ dual phase oxygen transport membranes, Journal of Membrane Science 544 (2017) 278-286.
[21] H. Luo, K. Efimov, H. Jiang, A. Feldhoff, H. Wang, J. Caro, CO_2-stable and cobalt-free dual-phase membrane for oxygen separation, Angewandte Chemie International Edition 50(3) (2011) 759-763.
[22] H. Luo, H. Jiang, K. Efimov, F. Liang, H. Wang, J.r. Caro, CO_2-tolerant oxygen-permeable Fe_2O_3-$Ce_{0.9}Gd_{0.1}O_{2-\delta}$ dual phase membranes, Industrial & Engineering Chemistry Research 50(23) (2011) 13508-13517.
[23] Z. Wang, W. Sun, Z. Zhu, T. Liu, W. Liu, A novel cobalt-free, CO_2-stable, and reduction-tolerant dual-phase oxygen-permeable membrane, ACS applied materials & interfaces 5(21) (2013) 11038-11043.
[24] H. Cheng, N. Zhang, X. Xiong, X. Lu, H. Zhao, S. Li, Z. Zhou, Synthesis, Oxygen Permeation, and CO_2-Tolerance Properties of $Ce_{0.8}Gd_{0.2}O_{2-\delta}$-$Ba_{0.95}La_{0.05}Fe_{1-x}Nb_xO_{3-\delta}$ Dual-Phase Membranes, ACS Sustainable Chemistry & Engineering 3(9) (2015) 1982-1992.
[25] X. Zhu, Y. Liu, Y. Cong, W. Yang, $Ce_{0.85}Sm_{0.15}O_{1.925}$-$Sm_{0.6}Sr_{0.4}Al_{0.3}Fe_{0.7}O_3$ dual-phase membranes: One-pot synthesis and stability in a CO_2 atmosphere, Solid State Ionics 253 (2013) 57-63.
[26] B. Wang, J. Yi, L. Winnubst, C. Chen, Stability and oxygen permeation behavior of $Ce_{0.8}Sm_{0.2}O_{2-\delta}$-$La_{0.8}Sr_{0.2}CrO_{3-\delta}$ composite membrane under large oxygen partial pressure gradients, Journal of Membrane Science 286(1-2) (2006) 22-25.
[27] S. Guo, Z. Liu, J. Zhu, X. Jiang, Z. Song, W. Jin, Highly oxygen-permeable and CO_2-stable $Ce_{0.8}Sm_{0.2}O_{2-\delta}$-$SrCo_{0.9}Nb_{0.1}O_{3-\delta}$ dual-phase membrane for oxygen separation, Fuel Processing Technology 154 (2016) 19-26.
[28] S.K. Kim, M.J. Shin, J. Rufner, K. van Benthem, J.H. Yu, S. Kim, $Sr_{0.95}Fe_{0.5}Co_{0.5}O_{3-\delta}$-$Ce_{0.9}Gd_{0.1}O_{2-\delta}$ dual-phase membrane: Oxygen permeability, phase stability, and chemical compatibility, Journal of Membrane Science 462 (2014) 153-159.
[29] S. Wang, T. Kobayashi, M. Dokiya, T. Hashimoto, Electrical and ionic conductivity of Gd-doped ceria, Journal of the Electrochemical Society 147(10) (2000) 3606-3609.

[30] Y. Ji, J.A. Kilner, M.F. Carolan, Electrical conductivity and oxygen transfer in gadolinia-doped ceria (CGO)-$Co_3O_{4-\delta}$ composites, Journal of the European Ceramic Society 24(14) (2004) 3613-3616.
[31] V. Kharton, A. Kovalevsky, A. Viskup, A. Shaula, F. Figueiredo, E. Naumovich, F. Marques, Oxygen transport in $Ce_{0.8}Gd_{0.2}O_{2-\delta}$-based composite membranes, Solid State Ionics 160(3-4) (2003) 247-258.
[32] A.J. Samson, M. Søgaard, P.V. Hendriksen, (Ce,Gd)$O_{2-\delta}$-based dual phase membranes for oxygen separation, Journal of Membrane Science 470 (2014) 178-188.
[33] V.V. Kharton, A.V. Kovalevsky, A.P. Viskup, F.M. Figueiredo, A.A. Yaremchenko, E.N. Naumovich, F.M.B. Marques, Oxygen Permeability of $Ce_{0.8}Gd_{0.2}O_{2-\delta}$-$La_{0.7}Sr_{0.3}MnO_{3-\delta}$ Composite Membranes, Journal of the Electrochemical Society 147(7) (2000) 2814-2821.
[34] U. Nigge, H.D. Wiemhöfer, E.W.J. Römer, H.J.M. Bouwmeester, T.R. Schulte, Composites of $Ce_{0.8}Gd_{0.2}O_{1.9}$ and $Gd_{0.7}Ca_{0.3}CoO_{3-\delta}$ as oxygen permeable membranes for exhaust gas sensors, Solid State Ionics 146(1-2) (2002) 163-174.
[35] Y. Lin, S. Fang, D. Su, K.S. Brinkman, F. Chen, Enhancing grain boundary ionic conductivity in mixed ionic-electronic conductors, Nature Communications 6(1) (2015) 6824.
[36] J. Garcia-Fayos, M. Balaguer, J.M. Serra, Dual-Phase Oxygen Transport Membranes for Stable Operation in Environments Containing Carbon Dioxide and Sulfur Dioxide, ChemSusChem 8(24) (2015) 4242-4249.
[37] H. Luo, H. Jiang, T. Klande, F. Liang, Z. Cao, H. Wang, J. Caro, Rapid glycine-nitrate combustion synthesis of the CO_2-stable dual phase membrane $40Mn_{1.5}Co_{1.5}O_{4-\delta}$-$60Ce_{0.9}Pr_{0.1}O_{2-\delta}$ for CO_2 capture via an oxy-fuel process, Journal of Membrane Science 423-424 (2012) 450-458.
[38] C. Zhang, J. Sunarso, S. Liu, Designing CO_2-resistant oxygen-selective mixed ionic-electronic conducting membranes: guidelines, recent advances, and forward directions, Chemical Society Reviews 46(10) (2017) 2941-3005.
[39] F. Zeng, J. Malzbender, S. Baumann, M. Krüger, L. Winnubst, O. Guillon, W.A. Meulenberg, Phase and microstructural characterizations for $Ce_{0.8}Gd_{0.2}O_{2-\delta}$-$FeCo_2O_4$ dual phase oxygen transport membranes, Journal of the European Ceramic Society 40(15) (2020) 5646-5652.
[40] F. Zeng, J. Malzbender, S. Baumann, A. Nijmeijer, L. Winnubst, M. Ziegner, O. Guillon, R. Schwaiger, W.A. Meulenberg, Optimization of sintering conditions for improved microstructural and mechanical properties of dense $Ce_{0.8}Gd_{0.2}O_{2-\delta}$-$FeCo_2O_4$ oxygen transport membranes, Journal of the European Ceramic Society 41(1) (2021) 509-516.
[41] F. Zeng, S. Baumann, J. Malzbender, A. Nijmeijer, L. Winnubst, O. Guillon, R. Schwaiger, W.A. Meulenberg, Enhancing oxygen permeation of solid-state reactive sintered $Ce_{0.8}Gd_{0.2}O_{2-\delta}$-$FeCo_2O_4$ composite by optimizing the powder preparation method, Journal of Membrane Science (2021) 119248.
[42] P.-M. Geffroy, J. Fouletier, N. Richet, T. Chartier, Rational selection of MIEC materials in energy production processes, Chemical Engineering Science 87 (2013) 408-433.
[43] S. Kim, S.H. Kim, K.S. Lee, J.H. Yu, Y.-H. Seong, I.S. Han, Mechanical properties of LSCF ($La_{0.6}Sr_{0.4}Co_{0.2}Fe_{0.8}O_{3-\delta}$)-GDC ($Ce_{0.9}Gd_{0.1}O_{2-\delta}$) for oxygen transport membranes, Ceramics International 43(2) (2017) 1916-1921.
[44] T. Nithyanantham, S. Biswas, N. Nagendra, S. Bandopadhyay, Studies on mechanical behavior of LSFT-CGO dual-phase membranes at elevated temperatures in ambient air and slightly reducing environments, Ceramics International 40(6) (2014) 7783-7790.
[45] S. Lia, W. Jin, N. Xu, J. Shi, Mechanical strength, and oxygen and electronic transport properties of $SrCo_{0.4}Fe_{0.6}O_{3-\delta}$-YSZ membranes, Journal of Membrane Science 186(2) (2001) 195-204.
[46] K. Raju, S. Kim, C.J. Hyung, J.H. Yu, Y.-H. Seong, S.-H. Kim, I.-S. Han, Optimal sintering temperature for $Ce_{0.9}Gd_{0.1}O_{2-\delta}$-$La_{0.6}Sr_{0.4}Co_{0.2}Fe_{0.8}O_{3-\delta}$ composites evaluated through their microstructural, mechanical and elastic properties, Ceramics International 45(1) (2019) 1460-1463.
[47] ASTM, C1322-15: Standard practice for fractography and characterization of fracture origins in advanced ceramics, ASTM International, West Conshohocken, PA, 2010.

[48] A. Lanin, Effect of residual stresses on the strength of ceramic materials, Russian Metallurgy (Metally) 2012(4) (2012) 307-322.
[49] F. Zeng, J. Malzbender, S. Baumann, F. Schulze-Küppers, M. Krüger, A. Nijmeijer, O. Guillon, W.A. Meulenberg, Micromechanical Characterization of $Ce_{0.8}Gd_{0.2}O_{2-\delta}$-$FeCo_2O_4$ Dual Phase Oxygen Transport Membranes, Advanced Engineering Materials 22(6) (2020) 1901558.
[50] F. Zeng, J. Malzbender, S. Baumann, W. Zhou, M. Ziegner, A. Nijmeijer, O. Guillon, R. Schwaiger, W.A. Meulenberg, Mechanical reliability of $Ce_{0.8}Gd_{0.2}O_{2-\delta}$-$FeCo_2O_4$ dual phase membranes synthesized by one-step solid-state reaction, Journal of the American Ceramic Society 00 (2020) 1-17.
[51] P.J. Murray, J.W. Linnett, Mössbauer studies in the spinel system $Co_xFe_{3-x}O_4$, Journal of Physics and Chemistry of Solids 37(6) (1976) 619-624.
[52] H. Bordeneuve, S. Guillemet-Fritsch, A. Rousset, S. Schuurman, V. Poulain, Structure and electrical properties of single-phase cobalt manganese oxide spinels $Mn_{3-x}Co_xO_4$ sintered classically and by spark plasma sintering (SPS), Journal of Solid State Chemistry 182(2) (2009) 396-401.
[53] M. Ramasamy, S. Baumann, J. Palisaitis, F. Schulze-Küppers, M. Balaguer, D. Kim, W.A. Meulenberg, J. Mayer, R. Bhave, O. Guillon, M. Bram, Influence of Microstructure and Surface Activation of Dual-Phase Membrane $Ce_{0.8}Gd_{0.2}O_{2-\delta}$-$FeCo_2O_4$ on Oxygen Permeation, Journal of the American Ceramic Society 99(1) (2016) 349-355.
[54] Y. Zheng, J.M. Vieira, F.J. Oliveira, J.P. Davim, P. Brogueira, Relationship between flexural strength and surface roughness for hot-pressed Si_3N_4 self-reinforced ceramics, Journal of the European Ceramic Society 20(9) (2000) 1345-1353.
[55] C.A. Schneider, W.S. Rasband, K.W. Eliceiri, NIH Image to ImageJ: 25 years of image analysis, Nature Methods 9(7) (2012) 671-675.
[56] M.E. Fitzpatrick, A.T. Fry, P. Holdway, F.A. Kandil, J. Shackleton, L. Suominen, Determination of residual stresses by X-ray diffraction, National Physical Laboratory, Teddington, UK, 2005.
[57] A. Atkinson, A. Selcuk, Mechanical behaviour of ceramic oxygen ion-conducting membranes, Solid State Ionics 134(1-2) (2000) 59-66.
[58] J.E. Choi, J.N. Waddell, M.V. Swain, Pressed ceramics onto zirconia. Part 2: indentation fracture and influence of cooling rate on residual stresses, Dental Materials 27(11) (2011) 1111-1118.
[59] G.R. Anstis, P. Chantikul, B.R. Lawn, D.B. Marshall, A critical evaluation of indentation techniques for measuring fracture toughness: I, direct crack measurements, Journal of the American Ceramic Society 64(9) (1981) 533-538.
[60] R.O. Silva, J. Malzbender, F. Schulze-Küppers, S. Baumann, O. Guillon, Mechanical properties and lifetime predictions of dense $SrTi_{1-x}Fe_xO_{3-\delta}$ (x = 0.25, 0.35, 0.5), Journal of the European Ceramic Society 37(7) (2017) 2629-2636.
[61] R. Bermejo, P. Supancic, C. Krautgasser, R. Morrell, R. Danzer, Subcritical crack growth in low temperature co-fired ceramics under biaxial loading, Engineering Fracture Mechanics 100 (2013) 108-121.
[62] ASTM, C1499-05: Standard test method for monotonic equibiaxial flexural strength of advanced ceramics at ambient temperature, ASTM International, West Conshohocken, PA, 2003.
[63] W.M. Harris, K.S. Brinkman, Y. Lin, D. Su, A.P. Cocco, A. Nakajo, M.B. DeGostin, Y.-c.K. Chen-Wiegart, J. Wang, F. Chen, Characterization of 3D interconnected microstructural network in mixed ionic and electronic conducting ceramic composites, Nanoscale 6(9) (2014) 4480-4485.
[64] K. Raju, S. Kim, J.H. Yu, S.-H. Kim, Y.-H. Seong, I.-S. Han, Rietveld refinement and estimation of residual stress in GDC-LSCF oxygen transport membrane ceramic composites, Ceramics International 44(9) (2018) 10293-10298.
[65] A. Moradkhani, H. Baharvandi, M. Tajdari, H. Latifi, J. Martikainen, Determination of fracture toughness using the area of micro-crack tracks left in brittle materials by Vickers indentation test, Journal of Advanced Ceramics 2(1) (2013) 87-102.

[66] B.X. Huang, J. Malzbender, R.W. Steinbrech, L. Singheiser, Discussion of the complex thermo-mechanical behavior of $Ba_{0.5}Sr_{0.5}Co_{0.8}Fe_{0.2}O_{3-\delta}$, Journal of Membrane Science 359(1) (2010) 80-85.
[67] B. Huang, J. Malzbender, R. Steinbrech, E. Wessel, H. Penkalla, L. Singheiser, Mechanical aspects of ferro-elastic behavior and phase composition of $La_{0.58}Sr_{0.4}Co_{0.2}Fe_{0.8}O_{3-\delta}$, Journal of Membrane Science 349(1-2) (2010) 183-188.